

WATER VAPOUR PROFILING USING LEO-LEO INTER-SATELLITE LINKS

Martin S. Lohmann⁽¹⁾⁽²⁾, Laust Olsen⁽¹⁾⁽³⁾, Hans-Henrik Benzon⁽¹⁾, Alan Steen Nielsen⁽¹⁾,
Arne Skov Jensen⁽¹⁾, Per Høeg⁽¹⁾

⁽¹⁾*Danish Meteorological Institute
Atmosphere Ionosphere Research Division
Lyngbyvej 100, DK-2100 Copenhagen Ø, Denmark*

⁽²⁾*Now at: University Corporation for Atmospheric Research
Boulder, Colorado, USA
Email: mlohmann@ucar.edu*

⁽³⁾*Corresponding author
Now at: Danish GPS Center, Aalborg University
Niels Jernes Vej 14, DK-9220 Aalborg Ø, Denmark
Email: lao@kom.auc.dk*

1. INTRODUCTION

Radio Occultation (RO) soundings of the Earth's atmosphere utilizing existing Global Navigation Satellite System (GNSS) signals has been carried out in several satellite missions starting with the GPS/MET experiment onboard the MicroLab 1 satellite [1]. These measurements provide information on the bending of the GNSS signals due to atmospheric refractive index variations. The bending information is used to retrieve vertical profiles of refractivity which in turn can be inverted to vertical profiles of pressure and temperature when the atmospheric water vapour content is negligible. When the water vapour contents cannot be neglected the water vapour profile can be obtained from a priori knowledge of the temperature.

Water vapour is a strong greenhouse gas and due to its large abundance it has significant influence on the climate. Also, due to the large energy transfers associated with the phase transitions of water it impacts the short term dynamics of the atmosphere considerably e.g. by stimulating the development of tropical hurricanes. Therefore an accurate knowledge of the temporal and spatial water vapour distribution is important for both climate research and weather prediction.

Recently improved RO missions with potential of independent retrieval of both temperature and humidity without a priori information has been proposed, see [2] and [3]. In the work presented here we simulate the concept of the proposed ACE+ mission, which include occultations between Low Earth Orbiting (LEO) satellites at three different frequencies around the 22.3 GHz water vapour absorption line. By measuring not only the phase but also the amplitude variations of the signals unambiguous retrieval of temperature and humidity profiles is made possible.

In this study we investigate the potential of the ACE+ system by performing end-to-end simulations using different realistic noise scenarios, the corresponding errors in temperature and humidity are presented and discussed.

2. END-TO-END SIMULATION SETUP

End-to-end simulations of LEO-LEO occultations require various steps of calculations, all illustrated in Fig.1. First, input geophysical parameters are transformed to a complex refractivity field using a Millimetre-wave Propagation Model (MPM). Subsequently, this complex refractivity field is applied in the wave optics propagation simulations that yield the electromagnetic field along the receiver orbit. Subsequently noise is added and bending angle and transmission profiles are retrieved and inverted into complex refractivity profiles through Abelian inversions. Finally, the profiles of geophysical parameters are retrieved through a non-linear least-square-fit. In the following these different processing steps are described.

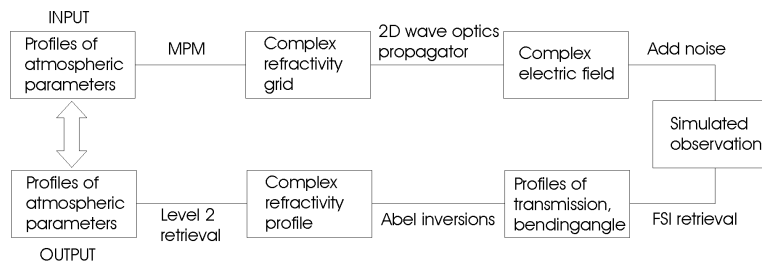


Fig.1. Overview of the simulation processing chain.

2.1. Atmosphere Model

The simulations presented in this study are based on a simple one-dimensional vertical model defining a smooth spherically symmetric atmosphere. The temperature model, $T(h)$, where h is geometric height, resembles the mean vertical structure of the Earth's atmosphere and is constructed by simple analytic expressions approximating the US Standard Atmosphere. The temperature model profile is shown in Fig.2 (left). The water vapour pressure model profile $e(h)$ is constructed by first specifying a linear variation in the relative humidity, RH , from 90% at the Earth surface decreasing to 0% at 10 km above the surface. Hence, the model atmosphere consists of a dry region above the tropopause and a humid region below the tropopause. Furthermore, no multipath phenomena are introduced since the refractivity gradient, due to water vapour variations, decreases with height. The relative humidity at each level is converted to the water vapour pressure profile shown in Fig.2 (right) using the following equations

$$RH = e / e_s \quad (1.a)$$

$$\log_{10} e_s = -\frac{2937.4}{T} - 4.9283 \cdot \log_{10} T + 23.5471 \quad (1.b)$$

[4] at each level; here e_s is the water vapour saturation pressure and T is the temperature. The total pressure model profile is calculated by specifying a surface pressure and assuming hydrostatic balance through a discrete version of

$$p(h) = p_0 \cdot \exp\left(-\int_0^h \frac{g}{RT(h')} dh'\right), \quad (2)$$

in which p_0 is the chosen surface pressure, g is the gravitational acceleration and R is the gas constant both taken to be constant. The quantities are calculated from 0 km to 130 km height at levels separated by 10 m.

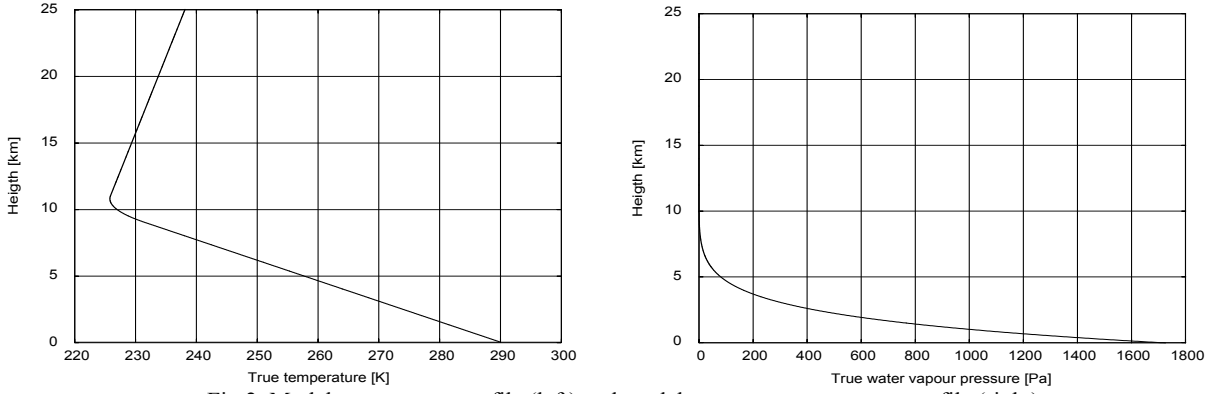


Fig.2. Model temperature profile (left) and model water vapour pressure profile (right).

Complex refractivity, $N(f)$, defined by $N(f) = (n(f) - 1) \cdot 10^6$ where n is the complex refractive index and f is frequency, is calculated using the Liebe Millimetre-wave Propagation Model (MPM) [5] for each of the frequencies 10, 17 and 23 GHz. In this study we assume that no liquid water is present and neglect the magnetic field influence on the refractivity. In Fig.3 (left) the real part of the refractivity is depicted. Only one curve is presented as the atmosphere is virtually non-dispersive for these frequencies. In Fig.3 (right) the imaginary refractivity is depicted for all three frequencies.

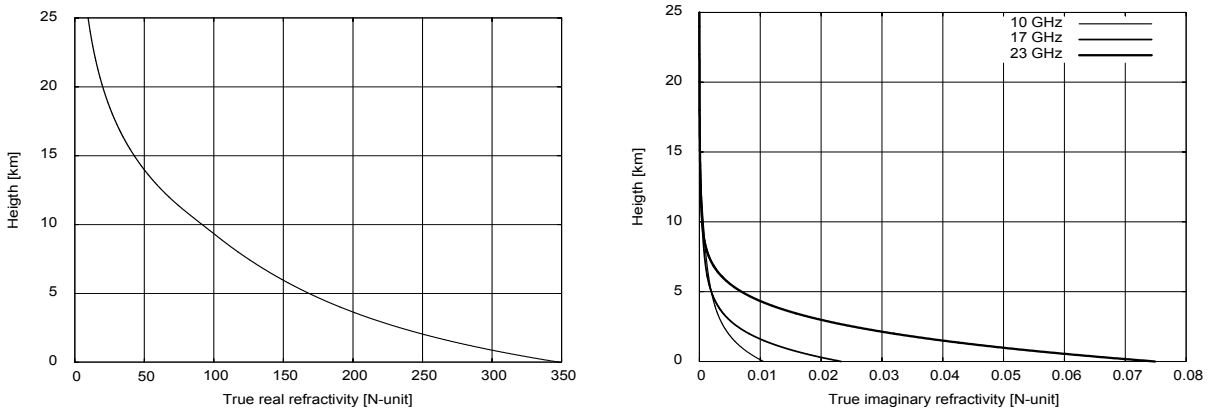


Fig.3. Model real refractivity (left) and model imaginary refractivities (right).

2.2 Signal Propagation

Simulation of the wave propagation through the atmosphere is based on the solutions to the Helmholtz wave equation. In this study these solutions are computed by solving the parabolic approximation to the Helmholtz wave equation. The primary limitations of this technique are that the backscattered field is neglected, and that accurate calculations are restricted to a small angular span around a preferred direction, in this case a near-horizontal direction. However, for the current study these limitations are not considered to have any measurable impact on the results. The Wave Optics Propagator (WOP) makes use of a ray tracer in order to locate the area to which the field propagation calculations can be confined [6].

The wave propagation simulation in the troposphere/stratosphere is based on the expansion of the field into a set of plane waves which are propagated through a set of parallel thin screens nearly orthogonal to the propagation direction. This is implemented using the fast Fourier transform (FFT) which significantly increases the execution speed of the propagator. Spatial frequencies are used in the Fourier transform calculations. Refraction is accounted for in the simulation by the specified real refractivity profiles on the screens whereas absorption is accounted for by specifying the imaginary refractivity on these screens.

The Earth is modelled including impedance giving a more accurate lower boundary condition [7]. The propagation of the wave field from the last screen to the LEO orbit is performed through a 2-D version of the Fresnel diffraction integral [8].

The satellite orbits considered in our simulations are circular orbits lying in the same plane where the transmitter and receiver are deployed at 850 and 650 km, respectively.

2.3 Noise simulation

All measurements are subject to noise. In LEO-LEO RO measurements thermal noise from the medium and in the receiver disturb the electromagnetic signal. We simulate these noise components by adding Gaussian white noise to the real and imaginary parts of the simulated electromagnetic field. In the simulations the power levels of the white noise series is set so that they correspond to pre-specified values of the *free space signal to noise density ratio* at the used sampling bandwidth. The free space signal to noise density ratio (SNR density) is the SNR per unit sampling bandwidth of the signal above the atmosphere, i.e. without atmospheric attenuation and defocusing. According to [2] the ACE+ instrument is expected to be designed so that the free space SNR density will be 66 dBHz which is currently the baseline for the ACE+ mission. We present simulations with free space SNR densities of 45, 56, 66, and 76 dBHz plus a noise free reference case.

2.4 Retrieval of Bending Angle and Transmission Based on FSI

Our retrieval scheme is based on the Full Spectrum Inversion (FSI) method [9]. The FSI technique applies a Fourier transform and uses the derivative of the phase after this transformation. Time and instantaneous frequency are the output from FSI – also in case of multipath, where there will be more Doppler frequencies at a given time. The Fourier amplitudes describe the distribution of energy with respect to impact parameter only modulated by signal spreading and absorption, i.e. defocusing is automatically accounted for.

When using Full Spectrum Inversion to invert radio occultation data, a distinction between ideal occultations and realistic occultations must be made. Ideal occultations are defined as occultations with a spherical Earth and perfect circular orbits lying in the same plane. On the other hand, realistic occultations are defined as occultations with an oblate Earth and approximately circular orbits lying in two different planes. In the former case, a global Fourier transform can be applied directly to the measured signal; and pairs of ray arrival time, t_0 , and ray Doppler angular frequency, ω_0 , is related through:

$$(\omega(t_0), t_0) = \left(\omega_0, - \left| \frac{d \arg(F)}{d\omega} \right|_{\omega=\omega_0} \right) \quad (3)$$

where F represents the Fourier transform of the measured signal.

Realistic occultations require that the occultation signal and ephemeris data are re-sampled with respect to the opening angle, θ , between the radius vectors of the satellites and that frequency variations caused by radial variations in the radius vectors are removed before the equation above is applied. Removal of those unwanted frequency variations requires a priori knowledge of the variations in impact parameter during an occultation, which can be estimated, e.g., from the smoothed signal phase [9]. When the variations in the Doppler frequency have been determined through (3), it is straightforward to compute the bending angle profile using standard retrieval techniques, see e.g. [10].

The corresponding transmission profile is determined by expressing the Fourier amplitudes with respect to impact parameter and by correcting the amplitudes for spreading modulations. The transmission, i.e. the normalized intensity, is related to the ray amplitude through

$$\xi(a) = \frac{I(a)}{I_m(a)} = \frac{A^2(a)}{A_m^2(a)} \quad (4)$$

where I is the intensity of the signal in the absence of spreading and defocusing, I_m is the intensity the signal would have had without absorption, spreading and defocusing, and A and A_m are the corresponding amplitudes. The Fourier amplitude is related to the occultation geometry through

$$|F(a)|^2 = \xi(a) \frac{P}{2\pi} \cdot \frac{a}{r_G r_L \sin(\theta) \sqrt{r_G^2 - a^2} \sqrt{r_L^2 - a^2} \left(\frac{d\theta}{da}\right)^2 k} \quad (5)$$

[9]. Here P is the transmitted power, r_G and r_L are the distances from the centre of curvature to the transmitter and receiver, respectively, and θ is the angle between these. This expression is valid in general for a 3-D geometry with circular orbits. For non-circular orbits additional terms are introduced in (5) as demonstrated in [11]. Since the simulated electromagnetic field is two-dimensional, spreading corrections are only performed for spreading within the occultation plane. Without transverse effects a factor of $a/(r_G r_L \sin(\theta))$ disappear from (5), see [12]. In this case the Fourier amplitude becomes

$$|F(a)|^2 = \xi(a) \frac{P}{2\pi} \cdot \frac{1}{\sqrt{r_G^2 - a^2} \sqrt{r_L^2 - a^2} \left(\frac{d\theta}{da}\right)^2 k} \quad (6)$$

where the transmitter power P is assumed to be constant throughout the occultation. From the following discussion it follows that a profile of transmission multiplied by the transmitted power is readily computed through (4) and (6). The transmitted power in the direction of the receiving satellite may not be known with a high accuracy, however, as long as the transmitted power is constant this will not affect the inversion; this will be shown in the following section.

The FSI method has a number of advantages related to LEO-LEO occultations:

- it disentangles multipath,
- defocusing is automatically accounted for,
- it does not require a coordinate transformation to fix the transmitting satellite,
- it is simple, both conceptually and computationally.

The major drawback of the FSI technique is that it relies on the assumption of local spherical symmetry. When this assumption is not fulfilled, the method may not be able to disentangle multipath. Like other methods based on Fourier operators, the FSI amplitude always suffers from minor amplitude oscillations caused by Gibb's phenomenon which may cause unwanted artificial oscillations in the retrieved transmission profiles [13]. The problem of Gibb's phenomenon can be solved by using appropriate window functions in the evaluation of the Fourier transform as described in [13]. We refer to this technique as the windowed FSI (WFSI). In the WFSI technique windows of the same form but with different durations are applied to the different components centred at the corresponding stationary phase points. The duration and position of the individual windows can be determined from a priori knowledge of the variations of the ray Doppler frequency. For practical applications this information can be obtained with sufficient accuracy from a standard FSI. This approach is also applied in this study. Due to the application of windows the WFSI method is also less sensitive to white noise compared to the standard FSI [13].

2.5 Retrieval of Complex Refractivity

Given profiles of bending angle and transmission as function of impact parameter the complex refractivity is derived. The real part of the refractivity is derived from the bending angle profile using the standard Abel inversion as described in e.g. [14]. Here, we will focus on retrieval of the imaginary part of the refractivity which is directly related to the absorption. The imaginary refractivity is given by

$$N'' = 10^6 \cdot n'' = 10^6 \cdot (2k)^{-1} \cdot \alpha \quad (7)$$

where k is the free space wave number, n'' is the imaginary part of the refractive index and α is the absorption coefficient per unit distance in the medium [15]. The absorption coefficient is calculated using an inverse Abel integral of the signal transmission, [3],

$$\alpha(a) = \frac{1}{\pi} \frac{da}{dr} \bigg|_{a'=a} \int_a^\infty \frac{d \ln \xi}{da} \frac{da'}{\sqrt{a'^2 - a^2}} \quad (8)$$

where r is the ray path perigee distance to the curvature centre, a is the impact parameter and ξ is the transmission defined in the previous section. From the equation above it follows that the transmission enters the Abel integral as the derivative of the logarithm of the transmission. The transmission may, therefore be scaled with any arbitrary constant without affecting the results of the Abel integral. This explains why it is not a problem for the inversion that the transmission derived from FSI is scaled by the unknown transmitted power as described in the previous section. The reason for this is that the signal absorption is related to the relative variations in the signal intensity and not the absolute variations. Consequently, there will be no need for calibration of the measured amplitudes as the observations will not be affected by long-term drifts in the instrument, which makes the technique very suitable for climate monitoring.

2.6 Retrieval of Geophysical Parameters

Given the retrieved profiles of both real and imaginary refractivity for the three frequencies proposed for the ACE+ mission, and assuming hydrostatic balance, we solve for dry pressure, temperature and water vapour pressure. Here we apply a solution procedure similar to the approach originally suggested in [12].

The three real refractivity profiles only constitute one piece of independent information as the atmosphere is virtually non-dispersive for the frequency range under consideration. Consequently, we have five pieces of independent information to solve for three unknowns. A least square (LS) fitting method is employed for this over-determined problem. It is worth to notice that if the signals had also been subject to absorption caused by liquid water, e.g. rain, we would have had to solve for an additional unknown parameter, liquid water. However, there will also in this case be a slight redundancy in the number of equations.

In order to exploit the information given by the hydrostatic equation in a simple manner, the inversion is started at the topmost layer corresponding to the largest altitudes where reliable observations can be achieved. Boundary conditions for the “unknown” parameters p , T and e are specified at this level. In the current simulations we have specified the “true” geophysical parameters as the upper boundary conditions. These parameters are also used to calculate an initial guess for the solution at the next level below. The initial guess is adjusted through minimization of a set of appropriate functions by the LS algorithm. The functions to be minimized reflect the information contained in the derived refractivities and the hydrostatic balance assumption. The function representing the hydrostatic balance constraint is implemented using

$$p_i = p_{i-1} + \Delta p \approx p_{i-1} + g \cdot \tilde{\rho}_i \cdot \Delta h_i = p_{i-1} + \frac{g}{2} \left(\frac{p_i}{RT_i} + \frac{p_{i-1}}{RT_{i-1}} \right) (h_i - h_{i-1}) \quad (9)$$

where ideal gas behaviour and linear density, ρ , variations between the levels have been assumed. The level index, i , is counted downwards from the topmost level and all other symbols have been declared in section 2.1 though it should be noted that here they refer to the retrieved atmospheric parameters and not to the input model parameters. Equation (9) expresses the bound on the solution at the i 'th level imposed by the solution from the level above. By re-arranging this expression and including the information from the retrieved refractivities we get the following cost function, $J(p_i, T_i, e_i)$, which must be minimized at each level with respect to the unknowns p_i , T_i and e_i :

$$\begin{aligned} J(p_i, T_i, e_i) = & \frac{1}{\sigma_{hy}^2} \left[\left(p_{i-1} + \frac{gp_{i-1}}{2RT_{i-1}} (h_i - h_{i-1}) \right) - \left(p_i - \frac{gp_i}{2RT_i} (h_i - h_{i-1}) \right) \right]^2 \\ & + (\sigma_{re}^2)^{-1} \cdot (N'_i - N'(p_i, T_i, e_i))^2 \\ & + (\sigma_{im,1}^2)^{-1} \cdot (N''_{i,1} - N''(p_i, T_i, e_i, f_1))^2 \\ & + (\sigma_{im,2}^2)^{-1} \cdot (N''_{i,2} - N''(p_i, T_i, e_i, f_2))^2 \\ & + (\sigma_{im,3}^2)^{-1} \cdot (N''_{i,3} - N''(p_i, T_i, e_i, f_3))^2 \end{aligned} \quad (10)$$

The first line in the cost function above represents the squared error in the hydrostatic balance equation where σ_{hy}^2 is the corresponding variance. The remaining terms represents the squared differences between the retrieved refractivities and the corresponding refractivities derived from the Liebe MPM model for p_i , T_i and e_i , weighted with the corresponding variances. In the Liebe model we neglect magnetic field, droplet density and rain rate contributions.

The cost function given by (10) is non-linear and is minimized using the Levenberg-Marquardt technique as implemented in the software package MINPACK [16]. In the solution procedure the retrieved geophysical parameters at one level is used as the initial guess at the next level and so on so forth. In the LS algorithm each function is weighted

by the variance of its corresponding data quantity as indicated in the equations above. In the simulations, fixed generic variances have been used at all levels and for all the simulations. A variance of 10^{-3} Pa^2 was used for the hydrostatic balance error function, a variance of 10^{-8} was used for the real refractivity function and a variance of 10^{-11} was used for all three cost functions related to the imaginary refractivity.

Since we have assumed that the liquid water content can be neglected in this study, there is some redundancy in this over-determined problem with five equations and three unknowns. The pieces of information that may be lost are one or more of the imaginary refractivities, as information from the real refractivity is only lost in the extreme situation where neither of the signals can be measured. The portions of the atmosphere where information from the imaginary refractivities could be lost are related to very wet or dry regions. In the lower troposphere, it is expected that the 23 GHz signal may be completely attenuated due to high concentrations of water vapour - this will especially be the situation in the tropics. In the upper troposphere the concentration of water vapour is expected to be so low that the absorption of the 10 GHz signal may not contain any useful information. This may also be the case for the other frequencies in the system when the atmosphere is very dry (for instance in the stratosphere), in these cases it will not be possible to retrieve the concentration of water vapour.

3. RESULTS AND DISCUSSION

The main purpose of this study has been to assess the impact of white noise for the retrieval chain described in the previous section. For the ACE+ mission the baseline signal-to-noise density is 66 dBHz [2]. Simulations have therefore been performed for different SNR densities around 66 dBHz, namely: 45 dBHz, 56 dBHz, 66 dBHz, 76 dBHz, and no noise. In the simulations the signals were sampled using a sampling frequency of 70 Hz, hence the lowest signal-to-noise density level of 45 dBHz, corresponds approximately to a SNR of 27 dB. Notice that these numbers corresponds to the free space signal strength as described in section 2.3. In the lower troposphere the signal decreases significantly due to both strong defocusing and strong absorption.

For the ACE+ mission the required vertical resolution is 500 m [2], hence a smoothing filter with vertical resolution of 500 m has therefore been applied in the retrieval chain.

It was found that for a given frequency and noise level the retrieved imaginary refractivity is subject to considerably larger relative errors than the corresponding real refractivity. The reason for this is that the relative variations in the ray phase induced by the atmosphere are larger than the relative variations in the ray amplitude induced by atmospheric absorption [13].

Fig.4 depicts the absolute and relative errors in the retrieved temperatures for the considered noise levels. The figure shows that the temperature errors increases with decreasing SNR, but it is also found that above 4 km the errors are nearly independent of height and do not exceed approximately 1 K for any of the considered noise scenarios. Below 4 km the temperature errors increases rapidly towards the surface. The height at which the errors start to increase depends on the SNR and decreases with increasing SNR. According to the ACE+ mission requirements the temperature root-mean-square (RMS) accuracy should be in the range of 0.5-2 K in the lower troposphere, 0-5 km, and in the range 0.5-1 K in the higher troposphere and lower stratosphere, 5-35 km, [17], which means that for the current simulations these error bounds are satisfied in the upper troposphere and lower stratosphere for all the considered noise cases whereas the error bound is exceeded in lower troposphere. The large errors in the lower troposphere are a consequence of the low SNR associated with observations of that part of the atmosphere where the signal is subject to both strong defocusing and strong absorption.

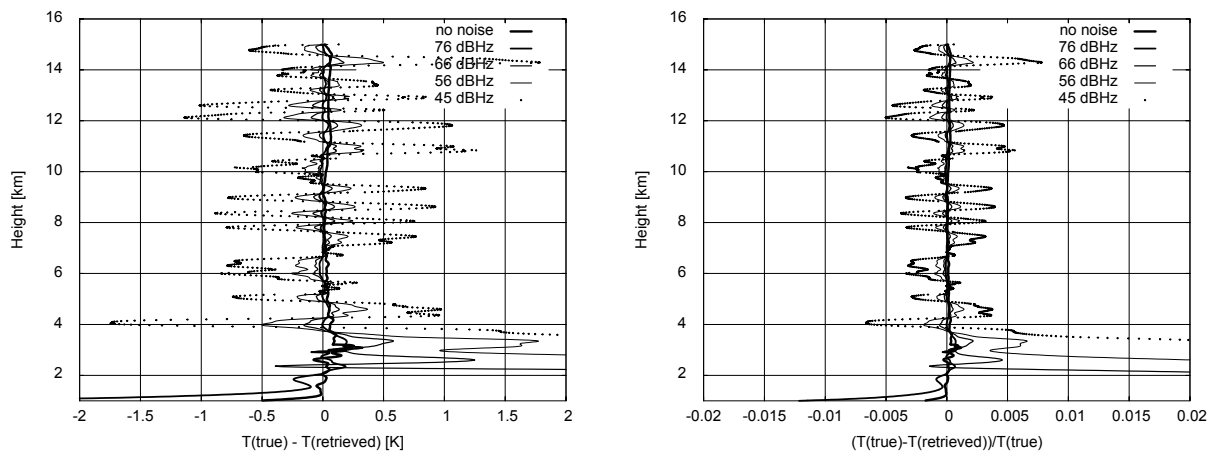


Fig.4. Absolute (left) and relative (right) error of retrieved temperature for the noise levels indicated.

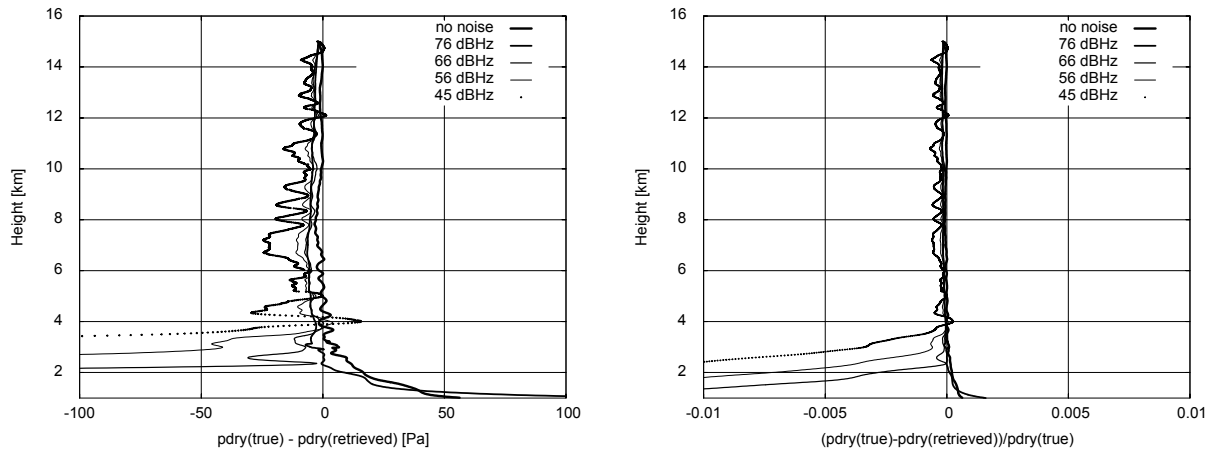


Fig.5. Absolute (left) and relative (right) error in retrieved dry pressure for the noise levels indicated.

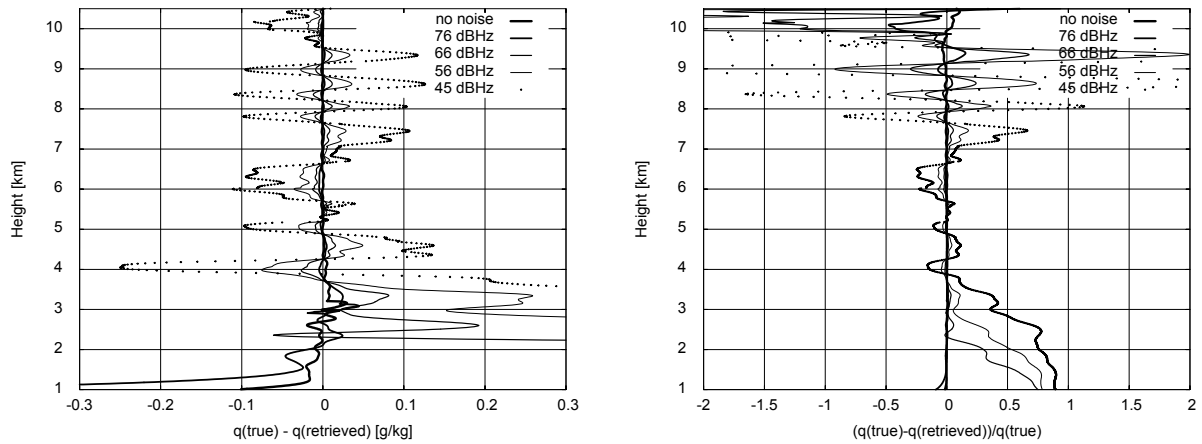


Fig.6. Absolute (left) and relative (right) error of retrieved specific humidity for the noise levels indicated.

In Fig.5 the absolute and relative errors in the retrieved dry pressure are shown. The pressure errors have the same trend as the temperature errors; the errors are small and independent of height except in the dense and moist lower troposphere where the errors increase towards the earth surface. Again, as for the temperature retrieval, the errors decrease significantly when SNR is increased

In Fig.6 the absolute and relative errors in the retrieved specific humidity are shown. Again we see the same trend as in the previous figures; the errors have strong dependence on the SNR, and also on height below 4 km. Above 4 km the absolute errors in specific humidity are nearly independent of height while the relative errors in specific humidity increase significantly with height above 7 km as a consequence of the very low water vapour contents in this part of the model atmosphere, see Fig.2. We can therefore conclude that the humidity retrieval has the best performance at heights of moderate water vapour content, which is in accordance with [18]. It is also worth to notice that even for the lowest SNR (45 dBHz) the absolute specific humidity errors do not exceed approximately 0.1 g/kg in upper troposphere. This is less than the RMS accuracies required for the ACE+ mission, which are 0.25-1 g/kg in the lower troposphere, 0-5 km, and 0.01-0.25 g/kg in the higher troposphere, 5-15 km, [17]. To summarize, the simulations presented in this study clearly indicates that mission requirements for the ACE+ mission can be met in the upper troposphere and lower stratosphere, but they also indicates that these error bounds may be exceeded in the lower troposphere due to high concentrations of water vapour. However, it should be noted that the simulations presented here do not include the effects of scintillations caused by small-scale irregularities in the atmosphere, e.g. turbulence, which may lead to increased fluctuations in phase and amplitude of the received signals [19].

4. CONCLUSION

In this study end-to-end simulations of LEO-LEO radio occultations have been performed using a set-up corresponding to the constellation planned for the ESA ACE+ mission with three frequencies located around the 22.3 GHz water

vapour absorption line. The main purpose of this study has been to demonstrate that in this set-up both temperature and humidity can be retrieved with an accuracy that satisfies the mission requirements for realistic signal to noise ratios. Simulations have been performed for different SNR density ratios around 66 dBHz being the baseline for the ACE+ mission. The simulations have been performed for a smooth spherical symmetric atmosphere resembling the US standard atmosphere with the addition of a very moist troposphere.

The results from the simulations have demonstrated the great potential of the ACE+ mission for retrieving independent information of both temperature and water vapour in the lower stratosphere and upper troposphere. But the simulations have also shown that the accuracy of the system can be significantly reduced by strong absorption and defocusing in the lower troposphere. In the lower stratosphere and upper troposphere both humidity and temperature can be retrieved within the error bounds stated in the ACE+ mission requirements even for the lowest considered signal to noise density of 45 dBHz. It was also found that in this part of the atmosphere the errors are nearly independent of height. In the lower troposphere the opposite is true and below a certain height, which depend on the SNR, the errors increases rapidly towards the surface. This increase in the errors is a result of the very moist troposphere considered in our simulations that give rise to both strong defocusing and significant absorption of the rays traversing the lower troposphere. Therefore, the signal corresponding to these rays will have very low SNR values which obviously lead to increased errors in the retrieved geophysical parameters.

5. REFERENCES

- [1] Ware, R., et al., "GPS Sounding of the Atmosphere from Low Earth Orbit: Preliminary Results," *Bull. Amer. Meteorol. Soc.*, 77(1), pp 19-40, 1996.
- [2] Høeg, P., and G. Kirchengast, "ACE+ Atmosphere and Climate Explorer based on GPS, GALILEO, and LEO-LEO Radio Occultation," Proposal to ESA in Response to the Second Call for Proposals for Earth Explorer Opportunity Missions, 2002.
- [3] Kursinski, E. R., et al., "A Microwave Occultation Observing System Optimized to Characterize Atmospheric Water, Temperature, and Geopotential via Absorption," *Journal of Atmospheric and Oceanic Technology*, 19, pp 1897-1914, 2002.
- [4] Salby, M. L., *Fundamentals of Atmospheric Physics*, Academic Press, 1995.
- [5] Liebe, H. J., "MPM - an Atmospheric Millimeter-wave Propagation Model," *International Journal of Infrared and Millimeter Waves*, vol. 10, No. 6, 1989.
- [6] Benzon, H.-H., A. S. Nielsen, and L. Olsen, "An Atmospheric Wave Optics Propagator - Theory and Application," *Danish Meteorological Institute Scientific Report 03-01*, Copenhagen, Denmark, 2003.
- [7] Levy, M., *Parabolic equation methods for electromagnetic wave propagation*, IEE, Electromagnetic waves series 45, 2000.
- [8] Gorbunov, M. E., A. S. Gurvich, and L. Bengtson, "Advanced algorithms of inversion of GPS/MET satellite data and their application to reconstruction of temperature and humidity," *Report 211*, Max-Planck-Institut für Meteorologie, Hamburg, Germany, 1996.
- [9] Jensen, A. S., M. S. Lohmann, H-H Benzon and A. S. Nielsen, "Full Spectrum Inversion of radio occultation signals," *Radio Sci.*, 38(3), 1040, doi:10.1029/2002RS002763, 2003.
- [10] Kursinski, E. R., G. A. Hajj, S. S. Leroy, and B. Herman, "The GPS Radio Occultation Technique," *TAO*, 11(1), pp 53-114, 2000.
- [11] Gorbunov, M. E., "Analysis of wave fields by Fourier Integral Operators and their application for radio occultations: Additional notes," unpublished, 2003.
- [12] Leroy, S. S., "Active Microwave Limb-sounding for Tropospheric Water Vapor: Some Theoretical Considerations," unpublished, 2001.
- [13] Lohmann, M. S., A. S. Jensen, H.-H. Benzon, and A. S. Nielsen, "Radio Occultation Retrieval of Atmospheric Absorption Based on FSI," *Danish Meteorological Institute Scientific Report*, in press, Copenhagen, 2003.
- [14] Fjeldbo, G., A. J. Kliore, and R. Eshlermann, The neutral atmosphere of Venus studied with the Mariner V radio occultation experiments, *Astron. J.*, 76(2), 123-140, 1971.
- [15] Born, M., and E. Wolf, *Principles of Optics*, Cambridge Univ. Press, New York, 1999.
- [16] <http://www.math.utah.edu/software/minpack/minpack/>.
- [17] ACE+ Observational/Main System Requirements, technical note, 2003.
- [18] Eriksson, P., C. Jimémez, D. Murtagh, G. Elgered, T. Kuhn and S. Bühler, "Measurement of tropospheric/stratospheric transmission at 10-35 GHz H₂O retrieval in low Earth orbiting satellite links," *Radio Sci.*, 38(4), 8069, doi:10.1029/2002RS002638, 2003.
- [19] Sokolovskiy, S., "Effect of Superrefraction on Inversion of Radio Occultation Signals in the Lower Troposphere," *Radio Sci.*, 38(3), 1058, doi:10.1029/2002RS002728, 2003.